Available online at www.sciencedirect.com
SCIENCE DIRECT®
Ocean Modelling 11 (2006) 69–97
Ocean Modelling
www.elsevier.com/locate/ocemod

Comparison of entrainment in overflows simulated by z-coordinate, isopycnal and non-hydrostatic models ☆

Sonya Legg [a,b,*,1,2], Robert W. Hallberg [b], James B. Girton [a,1,3]

[a] *Department of Physical Oceanography, Woods Hole Oceanographic Institution, Woods Hole, MA 02543, United States*
[b] *NOAA Geophysical Fluid Dynamics Laboratory, Princeton University, Forrestal Campus, US Rt 1, P.O. Box 308, Princeton, NJ 08542, United States*

Received 11 May 2004; received in revised form 23 November 2004; accepted 23 November 2004
Available online 13 January 2005

Abstract

A series of idealised numerical simulations of dense water flowing down a broad uniform slope are presented, employing both a z-coordinate model (the MIT general circulation model) and an isopycnal coordinate model (the Hallberg Isopycnal Model). Calculations are carried out at several different horizontal and vertical resolutions, and for a range of physical parameters. A subset of calculations are carried out at very high resolution using the non-hydrostatic variant of the MITgcm. In all calculations dense water descends the slope while entraining and mixing with ambient fluid. The dependence of entrainment, mixing and down-slope descent on resolution and vertical coordinate are assessed. At very coarse resolutions the z-coordinate model generates excessive spurious mixing, and dense water has difficulty descending the slope. However, at intermediate resolutions the mixing in the z-coordinate model is less than found in the high-resolution non-hydrostatic simulations, and dense water descends further down the slope.

☆ Woods Hole Oceanographic Institution Contribution 11263.

* Corresponding author. Address: NOAA Geophysical Fluid Dynamics Laboratory, Princeton University, Forrestal Campus, US Rt 1, P.O. Box 308, Princeton, NJ 08542, United States. Tel.: +1 609 452 6582; fax: +1 609 987 5063.
E-mail addresses: slegg@whoi.edu (S. Legg), robert.hallberg@noaa.gov (R.W. Hallberg), jgirton@whoi.edu (J.B. Girton).

[1] Supported in part by NSF grant 99858400 and the Gravity Current Entrainment Climate Process team funded by NSF grant 0336850.
[2] Supported in part by a UCAR visiting fellowship funded by NOAA.
[3] Supported by an NOAA Climate and Global Change Postdoctoral fellowship, administered by UCAR.

1463-5003/$ - see front matter
doi:10.1016/j.ocemod.2004.11.006

Isopycnal calculations show less resolution dependence, although entrainment and mixing are both reduced slightly at coarser resolution. At intermediate resolutions the z-coordinate and isopycnal models produce similar levels of mixing and entrainment. These results provide a benchmark against which future developments in overflow entrainment parameterizations in both z-coordinate and isopycnal models may be compared.

Keywords: Overflows; Entrainment; Vertical coordinate; Model resolution; Mixing parameterization

1. Introduction

Dense water formed through cooling or evaporation in marginal seas (e.g. the Greenland–Iceland–Norwegian sea, the Mediterranean, the Red sea) or on coastal shelves (e.g. the Arctic and Antarctic shelves) enters the general ocean circulation by flowing over topographic features, such as straits and sills (e.g. the Denmark Straits, Faroe Bank Channel, Gibraltar Straits, Bab-el-Mandab) and down the continental slope. These density driven currents flowing down topography are known as overflows. As the water descends it entrains ambient fluid, which mixes with the dense water, modifying the tracer properties and increasing the volume of the dense water mass (Price and Baringer, 1994). The overflow waters, modified by entrainment, include North Atlantic Deep Water (Dickson and Brown, 1994), Mediterranean Overflow Water (Price et al., 1993), and Antarctic Bottom Water (Gordon et al., 1998), and ultimately fill much of the abyssal ocean. Accurate representation of overflows and the entrainment they produce is therefore vital for correctly representing these deep water masses in ocean general circulation models.

It is now well known that different model formulations have different levels of success in representing overflows (Griffies et al., 2000). Of particular importance is the model's vertical discretization (Willebrand et al., 2001). Terrain-following coordinate models (e.g. the Princeton Ocean Model, http://www.aos.princeton.edu/WWWPUBLIC/htdocs.pom/, the Rutgers Ocean Modeling System (Haidvogel et al., 2000)) have the ability to concentrate resolution near the bottom boundaries, and hence can resolve overflow processes well, provided the vertical resolution is sufficiently fine. However, when topography is steep they have problems with pressure-gradient errors (Haney, 1991), although these are reduced but not eliminated by recent improved numerical schemes (Ezer et al., 2002; Shchepetkin and McWilliams, 2003). Isopycnal coordinate models (e.g. HIM (Hallberg and Rhines, 1996), MI-COM, http://oceanmodeling.rsmas.miami.edu/micom/) have no difficulties accurately representing topography, and are able to concentrate resolution in regions of large density gradients (often found at the interface between overflow waters and ambient fluid). In addition the diapycnal mixing and entrainment associated with the overflow can be explicitly parameterized (Hallberg, 2000; Papadakis et al., 2003). While isopycnal models and related hybrid coordinate models (e.g. HYCOM, http://oceanmodeling.rsmas.miami.edu/hycom/; Poseidon, http://www.scs.gmu.edu/climate/poseidon/) are increasingly being employed for climate studies, the majority of the established climate models (e.g. CCSM, http://www.ccsm.ucar.edu/; MOM, http://www.gfdl.noaa.gov/fms/pubrel/j/mom4/doc/mom4_manual.html) use height as their vertical coordinate. Height or z-coordinate models have particular difficulties in

representing overflows accurately. Unless both vertical and horizontal resolution are fine enough to resolve the overflow adequately:

$$\Delta z < h \quad \text{and } \Delta x < h/\tan\alpha, \tag{1}$$

respectively, where h is the thickness of the overflow, and α is the topographic slope angle, z-coordinate models are unable to transport dense fluid down the slope without excessive entrainment (Winton et al., 1998). These resolution requirements, especially for horizontal resolution, are about an order of magnitude higher than currently affordable for global climate models.

In all 3 model formulations, the processes responsible for entrainment are not resolved for climate scale simulations, and hence must be parameterized. In terrain-following and isopycnal coordinate models this is a relatively simple process of employing an appropriate diapycnal mixing parameterization. Currently several isopycnal coordinate models employ the empirical gravity current entrainment parameterization

$$\begin{aligned} W_e &= 0.1\Delta U \tfrac{0.8-Ri}{1+5Ri} \quad Ri < Ri_c \\ W_e &= 0 \qquad\qquad\qquad\quad Ri > Ri_c \end{aligned} \tag{2}$$

with $Ri_c = 0.8$, due to Ellison and Turner (1959), derived from non-rotating laboratory simulations of dense gravity currents on a slope in a uniform ambient fluid. Ellison and Turner (1959) use the bulk Richardson number $Ri = \Delta b h/(\Delta U)^2$ where Δb is the buoyancy anomaly of the gravity current, h is its depth and ΔU is the velocity difference between the gravity current and overlying fluid. In the implementation of this formula into isopycnal models such as HIM, a gradient Richardson number is used: $Ri = N^2/(\mathrm{d}u/\mathrm{d}z)^2$. Terrain-following coordinate models have tended to use turbulence closure schemes such as that due to Mellor and Yamada (1982).

In z-coordinate models a two-stage process is required to correctly represent overflow entrainment in coarse resolution models. First, a numerical scheme must be introduced to eliminate spurious mixing as dense fluid moves down topography. This ranges from crude ''plumbing'' models (Beckmann and Doscher, 1997; Campin and Goose, 1999), connecting grid-cells above and below a topographic step, to full bottom-boundary layer models (Killworth and Edwards, 1999; Song and Chao, 2000) which resemble a terrain-following coordinate region appended to the z-coordinate model. Second, the correct amount of entrainment has to be put back in, via a parameterization of small-scale processes (something only possible for the full bottom boundary layer models). For example, Killworth and Edwards (1999) employs a frictional bottom boundary layer model to determine the entrainment.

Currently there is an ongoing effort to evaluate these different methods of representing entrainment in overflows, and improve entrainment parameterizations to include additional physics, such as modifications of entrainment due to rotation and ambient stratification (the Gravity Current Entrainment Climate Process Team, http://www.cpt-gce.org). As part of this ongoing effort, we present here a comparison of numerical simulations of entraining overflows, employing a z-coordinate numerical model (MITgcm, http://mitgcm.org) without any bottom boundary layer model, and an isopycnal coordinate model (HIM, http://www.gfdl.noaa.gov/rwh/HIM/HIM.html). Most of the z-coordinate model simulations have sufficient resolution, as defined by criterion (1), to enable the plume to flow downslope without excessive entrainment, and in addition, like most z-coordinate simulations today, employ partial cell topography (Adcroft et al., 1997). The highest

resolution z-coordinate model simulations are non-hydrostatic and hence able to explicitly capture the largest-scale mixing processes responsible for entrainment. Our aims are: (a) to provide benchmark calculations, in the form of the highest resolution non-hydrostatic simulations, against which current and future parameterizations of entrainment can be compared; (b) to quantify how entrainment and diapycnal mixing in a z-coordinate model depends on resolution; (c) to provide a fair comparison between an isopycnal model (with explicit parameterization of diapycnal mixing) and z-coordinate model. The focus of this article is principally on the treatment of entrainment in overflows by models, rather than on the physical processes responsible for the entrainment, which are examined in detail in Girton and Legg (in preparation).

2. Model formulation

We employ one representative each of two different classes of model: the MITgcm, which uses height as the vertical coordinate, and the Hallberg Isopycnal Model (HIM). MITgcm (Marshall et al., 1997a,b) is unique in allowing comparison between calculations at both very coarse and very high resolution. At the highest resolutions non-hydrostatic physics are employed, and processes responsible for mixing are at least permitted, if not fully resolved. At the lowest resolutions, the model is hydrostatic, and convective adjustment is employed where needed to remove static instability. The model employs a conventional Arakawa C-grid at high resolutions, and the C–D scheme described in Adcroft et al. (1999) at coarse resolutions. At all resolutions partial step topography (Adcroft et al., 1997), a linear free-surface formulation, Laplacian friction (with a viscosity appropriate to the grid spacing), and quadratic bottom drag of $C_d = 2 \times 10^{-3}$ are employed. A direct discretization method with flux limiting is employed for tracers (Pietrzak, 1998), which both prevents the appearance of spurious oscillations while preserving fronts, and introduces numerical diffusion where needed for stability. Consequently we set the explicit tracer diffusion to zero, so that the background stratification is not eroded.

HIM solves the hydrostatic primitive equations in isopycnal coordinates. Even with the split-explicit time stepping scheme used here (Hallberg, 1997), HIM exactly conserves the mass of each isopycnal layer in the absence of explicitly parameterized diapycnal mixing. Diapycnal mixing is included using a weak background diffusivity of $10^{-4}\mathrm{m}^2\,\mathrm{s}^{-1}$ (of little significance to the result of these simulations) and the gradient-Richardson number mixing parameterization described by Hallberg (2000) derived from the bulk Richardson number entrainment parameterization of Turner (1986) and Ellison and Turner (1959), as well as a new bottom boundary mixing parameterization described in Appendix A. Topography is represented as a continuously varying field, and the pressure gradient discretization has in the past proven skillful for representing flows with isopycnals intersecting topography (Hallberg and Rhines, 1996). A biharmonic Smagorinsky viscosity is used as the momentum closure in the horizontal (Griffies and Hallberg, 2000). Bottom stress is parameterized with a quadratic drag law with $C_d = 2 \times 10^{-3}$ and a background velocity of $5\,\mathrm{cm\,s}^{-1}$. Tracers are advected along isopycnals with a monotonic and conservative flux-form scheme, following Easter (1993), and there is no explicit isopycnal tracer diffusion.

The idealized overflow scenario we have chosen to examine is shown in Fig. 1 and follows closely the scheme originally proposed by the Dynamics of Overflow Mixing and Entrainment (DOME) working group (http://www.rsmas.miami.edu/personal/tamay/DOME/dome.html). A

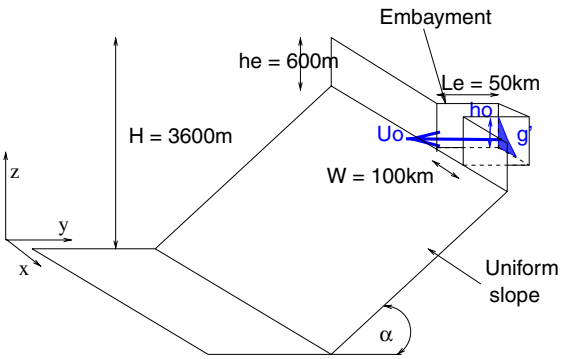

Fig. 1. Schematic showing the model domain, with the dense inflow entering in a flat bottomed embayment, which then opens onto the northern side of a uniform slope.

dense inflow is injected into the northern end of a flat-bottomed embayment of depth 600 m, and width 100 km, with a prescribed density and inflow speed. The embayment is 50 km long in the z-coordinate calculations and 100 km long in the isopycnal calculations. The embayment opens at its southern end onto a uniform slope to the south of angle α, which reaches a maximum depth of 3600 m, at which point there is a flat bottom.

The form of the dense inflow has been chosen (a) to be in geostrophic balance; (b) to have a maximum Froude number $Fr = U/\sqrt{(\Delta b h)}$ of 1 (where U is the velocity scale, Δb is the buoyancy anomaly and h is the thickness of the dense layer), such that $U_{\max} = \sqrt{\Delta b_0 h_0}$ where Δb_0 is the buoyancy anomaly of the inflow, and h_0 is the maximum height of the inflow above the bottom of the embayment; (c) to have a gradient Richardson number $Ri = N^2/(\mathrm{d}u/\mathrm{d}z)^2$ that is everywhere locally greater than 1/3 (well above the critical value), to minimize mixing in the embayment. The dense inflow has its maximum depth h_0 and maximum velocity at the right-hand wall (when looking downstream), and the inflow depth h decays exponentially with a lengthscale given by the deformation radius $L_\rho = \sqrt{\Delta b_0 h_0}/f$

$$h(x_{\mathrm{w}}) = h_0 \exp(-x_{\mathrm{w}}/L_\rho) \tag{3}$$

where x_{w} is the distance from the right-hand wall of the embayment. The above conditions are met by an inflow which has a buoyancy and velocity structure given by

$$b(x_{\mathrm{w}}, z) = \min(b_0 - \Delta b_0(1 - F(z^*)), b_0 - N^2 z) \tag{4}$$

$$v(x_{\mathrm{w}}, z) = -U_0 \exp(-x_{\mathrm{w}}/\mathrm{Ł}_\rho)(1 - F(z^*)) \tag{5}$$

where

$$U_0 = \sqrt{\Delta b_0 h_0} \tag{6}$$

and

$$z^*(x_w, z) = \frac{(z - h(x_{\mathrm{w}}) - h_{\mathrm{e}})}{h(x_{\mathrm{w}})} \tag{7}$$

with h_e the bottom depth of the embayment and

$$\begin{aligned} F(z^*) &= 1 && \text{for} \quad z^* \geqslant \tfrac{Ri_m}{2-Ri_m} \\ F(z^*) &= \tfrac{1}{Ri_m}\tfrac{z^*}{z^*+1} + \tfrac{1}{2} && \text{for} \quad -\tfrac{Ri_m}{2+Ri_m} < z^* < \tfrac{Ri_m}{2-Ri_m} \\ F(z^*) &= 0 && \text{for} \quad z^* \leqslant -\tfrac{Ri_m}{2+Ri_m} \end{aligned} \tag{8}$$

Ri_m is the minimum gradient Richardson number associated with the interface between the dense inflow and overlying water (set to $Ri_m = 1/3$). b_0 is the buoyancy value at the surface. The buoyancy structure is therefore set to $b = b_0 - \Delta b_0$ in most of the inflow, and to $b = b_0 - N^2 z$ in the overlying fluid, with a transition zone of a width and form designed to keep the gradient Richardson number above Ri_m. The velocity structure given by Eq. 5 is in fact in perfect geostrophic balance with the buoyancy only if $N^2 = 0$, but since Δb_0 is large compared to $N^2 h_0$, the discrepancy is not large. Ignoring the finite thickness of the interface, when $W \gg L_\rho$ the inflow transport is $T_{in} = \Delta b_0 h_0^2/(2f)$.

These conditions were chosen so that the structure of the inflow changes as little as possible within the embayment. For example, the $Fr = 1$ criterion was found to be necessary to prevent a Kelvin wave from propagating along the right-hand wall at a speed larger than the inflow speed, which causes excessive numerical entrainment in the first few grid points, to make up the necessary mass flux.

Within this basic structure, we have carried out simulations for six different combinations of parameters, described in Table 1. Case 1, which we term the reference case (*Ref*), has both rotation and ambient stratification. Case 2 ($0.5\Delta b_0$) and Case 3 ($0.1\Delta b_0$) differ from Case 1 only in the value of the background stratification, and the buoyancy anomaly of the inflow (one half and one tenth that of the reference case respectively); the density of the inflow matches the ambient density at the bottom of the slope in each case. Case 4 (*no f*) is as for Case 1, but with no rotation. Case 5 (*0.5 slope*) is as for Case 1, but with half the magnitude of topographic slope. Case 6 (*no* N^2) is as for Case 1 but without ambient stratification. Our rationale in choosing these different scenarios is

Table 1
Values of dimensional parameters

Dimensional parameter	Case 1 *Ref*	Case 2 $0.5\Delta b$	Case 3 $0.1\Delta b$	Case 4 *no f*	Case 5 0.5 slope	Case 6 *no* N^2
Inflow buoyancy anomaly Δb_0 (ms^{-2})	0.019	9.5×10^{-3}	1.9×10^{-3}	0.019	0.019	0.019
Inflow velocity amplitude U_0 (m/s)	2.4	1.7	0.75	2.4	2.4	2.4
Ambient stratification N (10^{-4} s^{-1})	23	16	7.2	23	23	0
Coriolis parameter f_0 (s^{-1})	10^{-4}	10^{-4}	10^{-4}	0	10^{-4}	10^{-4}
Topographic slope *tan* α	0.01	0.01	0.01	0.01	0.005	0.01

Dimensional parameter	Value
Inflow height h_0 (m)	300
Embayment width W (km)	100
Embayment depth h_e (m)	600
Embayment length L_e (km)	50
Maximum depth H (m)	3600
Drag coefficient C_d	2×10^{-3}

that we wish to examine how the models behave under a reasonable, but by no means exhaustive, variety of parameters. Case 4 (*no f*) without rotation, allows us to compare with much of the laboratory literature on entraining gravity plumes, most of which does not consider rotation. Case 6 (*no* N^2), without ambient stratification, allows us to compare with the recent laboratory experiments of Lane-Serff and Baines (1998) and Cenedese et al. (2004). Cases 2, 3 and 5 allow us to examine a little of the parameter space in the same regime as Case 1 (stratified and rotating) but with different degrees of rotational control, and different values of deformation radius.

For *no f* without rotation, the inflow height is constant with x_w at $h = h_0$, and the inflow velocity is given by

$$v(x_w, z) = -U_0(1 - F(z^*)) \tag{9}$$

independent of x_w. The total inflow transport in the non-rotating *no f* ($T_{in} = \sqrt{(\Delta b_0 h_0) h_0 W}$) is therefore considerably greater than in the rotating cases where v and h decrease away from the western wall.

Given the controlling parameters Δb_0, U_0, h_0, N^2, f_0, α, W, h_e, L_e, H, ν_h, ν_v and C_d, a total of 11 non-dimensional parameters are needed to fully describe the flow. However, given our six cases, we are obviously not exploring this parameter space in its entirety.

A particular choice of non-dimensional parameters appropriate to the rotating scenario is given in Table 2. Additional non-dimensional parameters needed to complete the set are the frictional Ekman number $\nu_v/(h_0^2 f_0)$ and the ratio ν_h/ν_v, both of which vary with resolution, and the geometrical ratios which are held fixed: $h_0/h_e = 0.5$, $L_e/W = 2.0$, $H/h_e = 6$. (The Reynolds number $U_0 h_0/\nu_h$ is also an important parameter, but is not independent of the parameters listed. Just as Ekman numbers for the simulations are larger than in the real ocean, so are the Reynolds numbers considerably smaller. By the above measure, in the z-coordinate calculations Re varies from 1400 for the highest resolution simulation down to 14 for the lowest resolution calculation. The isopycnal-coordinate calculations use a variable horizontal viscosity, so *Re* is not a well-defined external parameter.) The principal parameters we vary are the stretching parameter: $\Gamma = L_\rho \tan\alpha/h_0$; the channel width relative to the deformation radius: W/L_ρ; the Ekman numbers and the ratio N/f. Case 4 (*no f*) with zero rotation lies at one extreme for the rotation dependent parameters, while *no* N^2 lies at one extreme for the parameters dependent on ambient stratification (e.g. relative buoyancy anomaly, N/f). For comparison with other studies, we note that Cenedese et al. (2004) find that eddies are replaced by laminar flow for frictional Ekman numbers >0.1, while Lane-Serff and Baines (1998) find that $\Gamma > 0.1$ is necessary for the development of eddies

Table 2
Nondimensional parameter definitions and values for the different scenarios

Nondimensional parameter	Case 1 *Ref*	Case 2 $0.5\Delta b$	Case 3 $0.1\Delta b$	Case 4 *no f*	Case 5 0.5 slope	Case 6 *no* N^2
Froude number $U_0/\sqrt{(\Delta b_0 h_0)}$	1	1	1	1	1	1
Relative buoyancy anomaly $\Delta b_0/(N^2 h_0)$	12	12	12	12	12	∞
Stretching parameter $L_\rho \tan\alpha/h_0$	0.8	0.5	0.26	∞	0.4	0.8
Relative width $W/L_\rho = Wf_0/\sqrt{(\Delta b_0 h_0)}$	4.1	5.9	13.2	0	4.1	4.1
N/f	23.0	16.2	7.2	∞	23.0	0
Drag Ekman number $C_d \Delta b_0 \tan\alpha/(f_0^2 h_0)$	0.127	0.063	0.0127	∞	0.063	0.127

(although they do not consider $\Gamma > 1.0$, when we might expect rotational effects to diminish). (Note that although Lane–Serff and Baines define their stretching parameter slightly differently, for our model set up with $h_0 = h_e - h_0$, the two definitions give the same value.)

Our particular choice of dimensional parameters for the suite of simulations was selected to cover the values that are typical of oceanic overflows such as the Denmark Straits Overflow, the Mediterranean Outflow, the Red Sea Outflow, and some of the Antarctic overflows, although with the linear background stratification and linear slope the correspondence between these idealized simulations and the real observations is not expected to be especially close. Given these parameters, we find that a domain of the order of $L_x \times L_y \times L_z = 1000$ km–2000 km $\times$ 600 km $\times$ 3600 m is necessary to capture the full mixing, descent to neutral stability level and detrainment of the plume from the topography. The precise values of the domain size in fact vary with resolution, since the amount of mixing, and hence neutral buoyancy level, is found to be a function of resolution. With the z-coordinate model we have carried out simulations at four different resolutions, as listed in Table 3, along with accompanying values of v_h and v_v, and resolution dependent non-dimensional parameters. At the very highest resolution, $\Delta x = \Delta y = 500$ m, $\Delta z = 30$ m, only three simulations are performed, for cases 1, 4, and 6, while at the other resolutions all six cases are calculated. For the higher resolutions of $\Delta x = 500$ m and $\Delta x = 2.5$ km, stretched grids are employed in the horizontal, so that the resolution coarsens approaching the Eastern, Western and Southern boundaries, allowing larger domains so that boundary effects on the overflow are minimized, while focusing resolution on the active part of the flow. Note that even at the highest resolution, we are far from achieving what might be estimated to be necessary to fully resolve the dominant straining flows responsible for mixing at the interface between overflow and ambient fluid—if the horizontal length scale of mixing was of the order of the vertical depth of the plume (e.g. 300 m), we would like a horizontal resolution of order 30–50 m, considerably less than the 500 m we employ. This however, would be impossible to achieve while simultaneously capturing the full descent of the plume to neutral stability level, and the mesoscale eddy activity associated with the plumes, given current computing resources. Isopycnal model calculations are carried out with horizontal resolutions of $\Delta x = 10$ km and 50 km, with 25 evenly spaced isopycnal layers between the surface density and the overflow maximum density. In isopycnal

Table 3
The cases run at each resolution and for each model type, and dimensional and non-dimensional resolution dependent parameters

$\Delta x \times \Delta z, \Delta b_l$	500 m $\times$ 30 m MIT gcm	2.5 km $\times$ 60 m MITgcm	10 km $\times$ 144 m MITgcm	50 km $\times$ 144 m MITgcm	10 km $\times$ Δb/24 HIM	50 km $\times$ Δb/24 HIM
Case 1 (*Ref*)	X	X	X	X	X	X
Case 2 ($0.5\Delta b$)	–	X	X	X	X	X
Case 3 ($0.1\Delta b$)	–	X	X	X	X	X
Case 4 (*no f*)	X	X	X	X	X	X
Case 5 (0.5 *slope*)	–	X	X	X	X	X
Case 6 (*no* N^2)	X	X	X	X	X	X
v_h (m^2 s^{-1})	5.0×10^{-1}	5.0	5.0×10^{1}	5.0×10^{1}	Variable	Variable
v_v (m^2 s^{-1})	1.0×10^{-2}	5.0×10^{-2}	5.0×10^{-1}	5.0×10^{-1}	10^{-4}, 5×10^{-1}	10^{-4}
$Ek = v_v/(h_0^2 f_0)$	0.0011	0.0055	0.055	0.055	0.000011, 0.055	0.000011
v_h/v_v	50	100	100	100	Variable	Variable

calculations, the background vertical viscosity is 10^{-4} m^2 s^{-1}, but where *Ri* is small very high values of ν_v are used.

Boundary conditions are as follows. In both model formulations, no-slip and no-flux boundary conditions are applied at the topography. The no-slip boundary condition adds an additional stress in the bottom grid cell on top of that implied by the quadratic bottom drag: the total stress is of the form

$$\tau_{i,3} = \left(2\frac{\nu_v}{\Delta z} + C_{\mathrm{d}}\sqrt{2\mathrm{KE}}\right)v_i \tag{10}$$

where KE is the horizontal kinetic energy at that point, and $(v_1, v_2) = (u, v)$, the horizontal velocity vector. (See the documentation of the MITgcm, http://mitgcm.org, for more details.) At the Northern boundary of the embayment a prescribed inflow open boundary condition is prescribed. In most simulations with the *z*-coordinate model an Orlanski radiative boundary condition is applied at the Western open boundary, in order to allow the dense plume to escape the domain (with rotation the plume propagates principally to the West along the topography), while at the Southern and Eastern boundaries there is a vertical wall. For the non-rotating simulations (*no f*), the Southern boundary is open, with the Orlanski radiative boundary condition (Orlanski, 1976), and the Eastern and Western boundaries are vertical walls, since without rotation the plume propagates directly south. In the isopycnal-coordinate simulations, there is a net input of mass and the sea level slowly rises throughout the simulation (the basin is made large enough that this trend in the sea level does not appear to affect the quasi-equilibrium state). Along the eastern and western walls, a sponge-layer is used to damp the density structure back toward the ambient state and remove the passive tracer that marks the plume.

3. Results: non-hydrostatic simulations

We will first describe the features of the flow in the three highest resolution non-hydrostatic simulations, for Cases 1 (*Ref*), 4 (*no f*), 6 (*no* N^2), respectively. In all our simulations we distinguish between the overflow water and the ambient fluid by use of a passive tracer, whose concentration τ is zero in the ambient fluid, and unity in the inflow dense water. Dilution of the tracer concentration therefore helps to illustrate the mixing in of ambient fluid, while we can easily define the boundary of the overflow by a surface such as $\tau = 0.01$. (This choice of cutoff is somewhat arbitrary, but the results are not sensitive to the precise value so long as it is small but non-zero.)

3.1. Case 1 (Ref): with rotation and ambient stratification

Fig. 2 shows snapshots of the tracer concentration (a) at the layer just above the bottom topography, and (b) in a vertical slice near the inflow. Qualitative features of note are the deflection of the dense fluid in the along-slope direction induced by rotation, and the growth of large amplitude eddies, as expected from previous studies (Jiang and Garwood, 1996; Lane-Serff and Baines, 1998, 2000; Cenedese et al., 2004). From Fig. 2(a) we see that most of the tracer dilution occurs just after the overflow enters the slope, with little mixing to the west of $x = -150$ km. Further to the west there is stirring generated by large amplitude eddies, but this does not appear to modify tracer

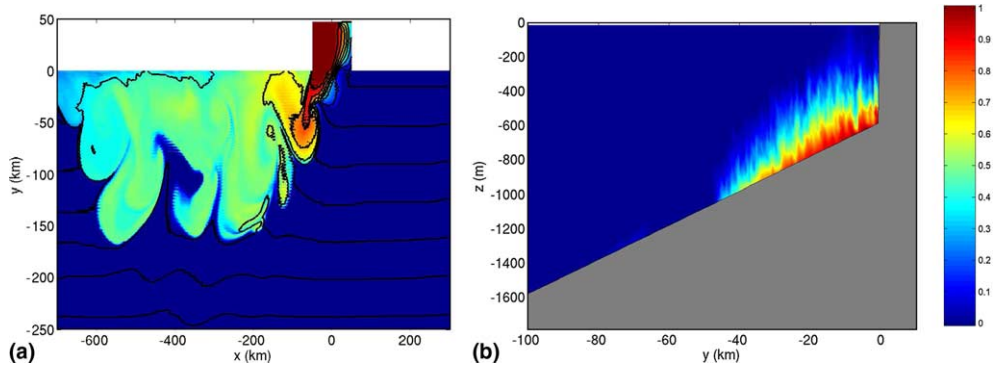

Fig. 2. Passive tracer concentration τ at a time 13 days after the initiation of the dense inflow, for Case 1 (*Ref*), at a resolution of $\Delta x \times \Delta z = 500\ \text{m} \times 30\ \text{m}$, simulated by the non-hydrostatic MITgcm: (a) τ just above the topography, as a function of horizontal distance, with buoyancy contours overlain; (b) τ in a vertical slice at $x = -50$ km, near the inflow. τ has a value of zero in the ambient fluid, and $\tau = 1$ in the inflow. The same tracer color scale is used in all subsequent similar images.

concentrations significantly. The superimposed buoyancy contours show that once the overflow water has spread cross-slope to about $y = -150$ km it has reached its neutral buoyancy level (there are no buoyancy contours separating high τ overflow fluid from the zero τ ambient fluid). Fig. 2(b) demonstrates the small-scale structures near the inflow responsible for mixing. While of a scale greater than the gridscale, it is likely that these are only a poorly resolved version of shear instability, so we refer to these simulations as "mixing-permitting" rather than "mixing-resolving". Nonetheless this resolution is the maximum possible with current computing facilities: a total of $nx \times ny \times nz = 888 \times 600 \times 120$ grid points were used, and the calculation required 30,000 h of CPU time running on 480 processors of the GFDL NOAA SGI Origin supercomputer.

By defining all fluid with $\tau > 0.01$ as the overflow, we can calculate the total transport in the along-slope direction as

$$T(x) = \int_A U\,\mathrm{d}y\,\mathrm{d}z: \text{ where } A \text{ is such that } \tau > 0.01 \tag{11}$$

and U is the zonal velocity. Fig. 3(a) shows the instantaneous along-slope transport as a function of along-slope distance for several different times, with the time-mean transport overlain. (These values are not significantly altered by choosing a somewhat higher or lower threshold tracer concentration to define the plume.) We see that for locations to the east of $x = -400$ km, an approximately steady-state is reached, although with large temporal fluctuations associated with the eddy activity. To the west of $x = -400$ km the flow is still evolving as the overflow water moves out of the domain.

Fig. 3(b) shows the entrainment coefficient deduced from the time-mean transport, for the region west of the inlet entrance at $x = -50$ km. The entrainment coefficient is diagnosed as

$$\alpha_{\mathrm{E}}(x) = \frac{\frac{\mathrm{d}}{\mathrm{d}x}T(x)}{L\overline{U}} \tag{12}$$

where L is the length of the interface between overflow water ($\tau > 0.01$) and ambient water in the (y,z) plane, and $\overline{U}$ is the average velocity defined by

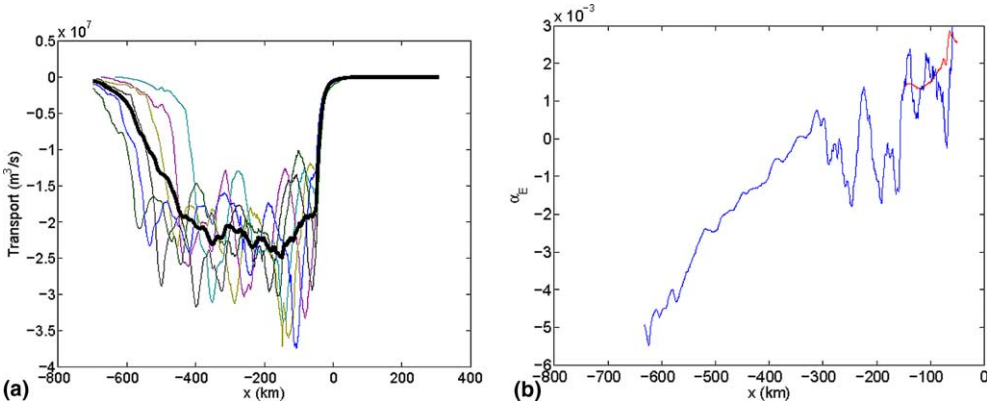

Fig. 3. For Case 1 (*Ref*), simulated at a resolution of $\Delta x \times \Delta z = 500\ \text{m} \times 30\ \text{m}$ with the non-hydrostatic MITgcm: (a) the total along-slope transport in the overflow fluid (identified by $\tau > 0.01$), as a function of along-slope distance (with the center of the inlet at $x = 0$). Several instantaneous values of transport are shown (at time intervals of 1.16 days), with the mean of these values overlain as a thick solid line and (b) the entrainment coeffcient diagnosed from the time-mean transport, for the region west of the inlet entrance at $x = -50$ km, as a function of along-slope distance. The small segment in red from -180 km $< x < -50$ km corresponds to the entrainment deduced from a linear fit to the actual time–mean transport between those points.

$$\overline{U} = \frac{\int_A U\,\mathrm{d}y\,\mathrm{d}z}{A} \tag{13}$$

We see that the entrainment coefficient is only finite and positive over a distance -200 km $< x < -50$ km, beyond which entrainment is zero to within the error set by the large fluctuations, and then negative (detrainment) in the region where a steady-state has not yet been reached. While this calculation only gives entrainment for the region west of $x = -50$ km, much of the mixing (as shown in Fig. 2(a)) occurs in the corner region bounded by $y = 0$ km and $x = -50$ km, and it is likely that this is also a region of significant increase in transport and hence entrainment. For this region we calculate a mean entrainment coefficient, defined as

$$\alpha_{\mathrm{E}} = \frac{\overline{T_{\mathrm{out}}}^{t} - \overline{T_{\mathrm{in}}}^{t}}{\overline{U_{\mathrm{rms}}}^{t}\,\overline{S}^{t}} \tag{14}$$

where T_{out} is the transport $\tau > 0.01$ water through $x = -50$ km, T_{in} is the transport $\tau > 0.01$ water through $y = 0$ km, S is the surface area of the $\tau = 0.01$ surface within this corner region, and U_{rms} is the rms horizontal velocity scale within the corner region. The time average $\overline{\ }^{t}$ of all quantities, once they have reached a statistically steady-state, is used. The average entrainment coefficient in this corner region is then 8.6×10^{-4}, of the same order of magnitude as the value just west of the corner. We also calculated the average entrainment over the length of the inlet, and found it to be negligible, so that mixing and entrainment both result only when the dense inflow encounters the slope.

While entrainment, as defined above, indicates an increase in the volume flux of $\tau > 0.01$ water, it does not give any information on the density of the entrained ambient fluid, and in particular whether the entrainment occurs across or along isopycnal surfaces. To demonstrate diapycnal mixing, we show in Fig. 4 the total amount of tracer, temporally averaged over the latter half

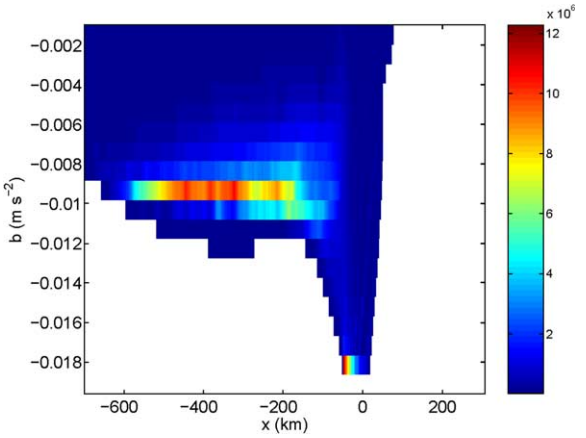

Fig. 4. The total tracer τ as a function of along-slope distance and buoyancy class, time-averaged over the latter half of the simulation, for Case 1 (*Ref*), simulated at a resolution of $\Delta x \times \Delta z = 500\ \text{m} \times 30\ \text{m}$ with the non-hydrostatic MITgcm.

of the simulation, as a function of along-slope distance and buoyancy. At the inflow location ($x = 0$) most tracer is found at a buoyancy of $b < -0.018\ \text{m/s}^2$. As the overflow moves along the slope, the maximum in tracer moves rapidly to lighter buoyancy classes. After $x = -200$ km the tracer maximum is at $-0.01 < b < -0.009\ \text{m/s}^2$, and beyond this there is no change in the location of tracer in buoyancy space. Hence we deduce that all the diapycnal mixing occurred to the east of $x = -200$ km. This coincides with the region of significant entrainment - hence the entrainment is largely diapycnal. Along isopycnal entrainment by the eddies appears to be insignificant, in terms of changing the net along-slope transport, perhaps because eddies serve to carry fluid off shore, rather than increase its advection along-slope.

A snapshot of the local gradient Richardson number $Ri = (\mathrm{d}b/\mathrm{d}z)/[(\mathrm{d}u/\mathrm{d}z)^2 + (\mathrm{d}v/\mathrm{d}z)^2]$ in a vertical slice at $y = -52$ km (Fig. 5) shows that Richardson numbers are small (<0.25) near the bottom from the inflow right to the western edge of the overflow. However, the superimposed buoyancy contours show that it is only for $x > -200$ km that finite buoyancy stratification coincides with the low Richardson numbers. Hence the entrainment and diapycnal mixing occur when low Richardson numbers coincide with finite positive vertical buoyancy gradients.

3.2. Case 4 (no f): without rotation, with ambient stratification

We now compare the rotating *Ref* with the non-rotating *no f*. All parameters are kept the same apart from Coriolis. The qualitative differences are large, as seen in the snapshots in Fig. 6. The dense current flows straight down the slope, and retains a symmetric shape about the middle axis of the inlet. A vertical section through the center of the dense flow (Fig. 6(a)) shows that there is small-scale mixing over the upper half of the slope, diluting the tracer concentration and a small overshoot beyond the neutral buoyancy level at depth. Following a rebound to neutral buoyancy level which has the character of an internal hydraulic jump, and may be associated with a transition from supercritical to subcritical flow, the overflow water flows out directly southward as a broad layer at its neutral buoyancy level. The three-dimensional character of the small-scale

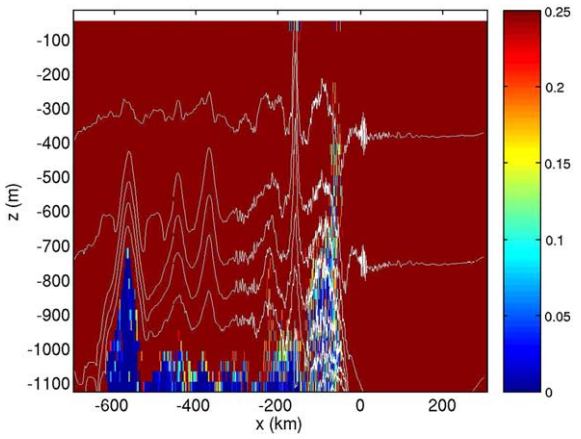

Fig. 5. The instantaneous local gradient Richardson number defined by $Ri = (\partial b/\partial z)/(\partial U/\partial z)^2$ in a vertical plane at $y = -52$ km and a time of $t = 13$ days, for Case 1 (*Ref*), simulated at a resolution of $\Delta x \times \Delta z = 500\ \text{m} \times 30\ \text{m}$ with the non-hydrostatic MITgcm.

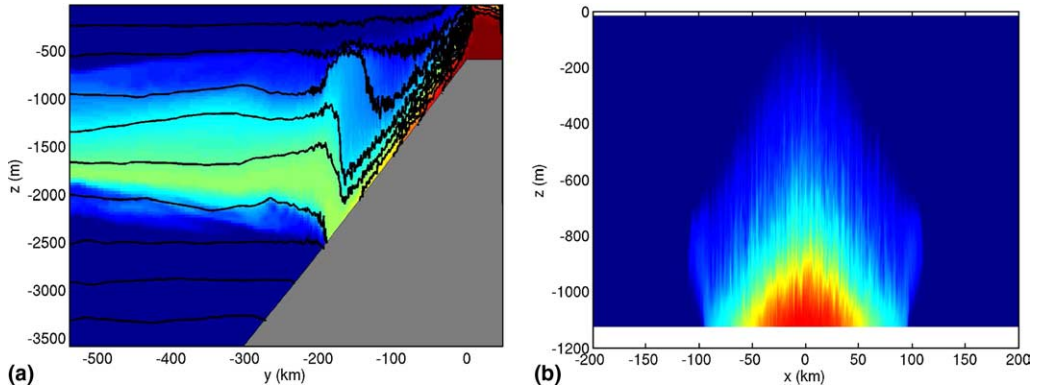

Fig. 6. Passive tracer concentration τ at a time 13 days after the initiation of the dense inflow, for Case 4 (*no f*), at a resolution of $\Delta x \times \Delta z = 500\ \text{m} \times 30\ \text{m}$, simulated by the non-hydrostatic MITgcm: (a) τ in a vertical slice at $x = 0$, with buoyancy contours overlain and (b) τ in a vertical slice at $y = -50$ km, near the top of the slope.

mixing is shown in the vertical cross-section taken near the top of the slope in Fig. 6(b). These flow features are as expected from previous studies of non-rotating gravity currents (Baines, 2001; Ellison and Turner, 1959).

For the non-rotating case, we estimate entrainment from the transport in the cross-slope direction, since the flow does not alter its course from that of the initial inflow. Fig. 7(a) shows the instantaneous cross-slope transport for several different times

$$T(y) = \int_A V \,\mathrm{d}x\,\mathrm{d}z : \text{ where } A \text{ is such that } \tau > 0.01 \tag{15}$$

where V is the cross-slope velocity. The transport magnitude increases mono-tonically down the slope, until neutral buoyancy is reached, when it remains approximately constant. The

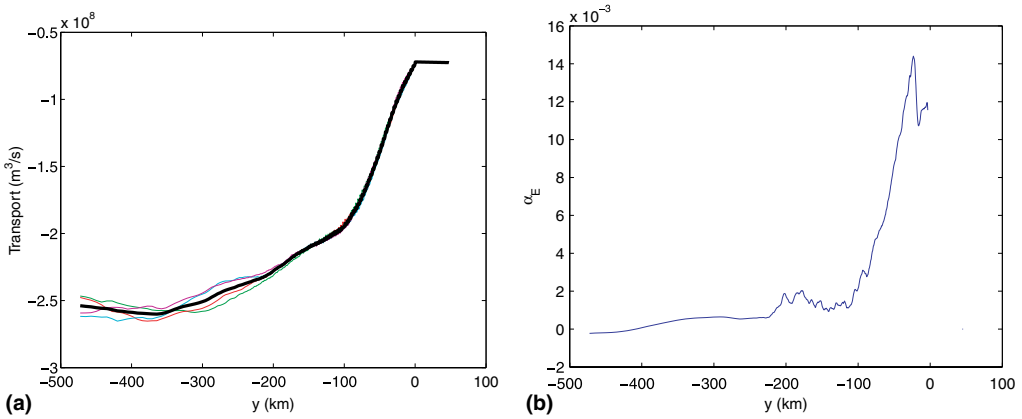

Fig. 7. For Case 4 (*no f*), simulated at a resolution of $\Delta x \times \Delta z = 500\ \mathrm{m} \times 30\ \mathrm{m}$ with the non-hydrostatic MITgcm: (a) the total cross-slope transport in the overflow fluid (identified by $\tau > 0.01$), as a function of cross-slope distance (with the beginning of the slope at $y = 0$ km). Several instantaneous values of transport are shown (at time intervals of 1.16 days), with the mean of these values overlain as a thick solid line and (b) the entrainment coefficient diagnosed from the time-mean transport, as a function of cross-slope distance.

entrainment deduced from the mean transport, shown in Fig. 7(b) shows a maximum at the top of the slope, decreasing monotonically to zero at the neutral buoyancy level.

The total tracer, as a function of cross-slope distance and buoyancy class is shown in Fig. 8. As in *Ref*, at the inflow, and until the top of the slope, most tracer is at a buoyancy of $b < -0.018$ m/s^2. As the overflow descends down the slope, mixing moves the tracer maximum to lighter buoyancy levels, and beyond $y = -150$ km most tracer is found in a broad band from $-0.01 < b < -0.005$ m/s^2.

The local gradient Richardson number, shown in a vertical plane through the center of the plume (Fig. 9) shows that low Richardson numbers are found over the whole dense overflow until

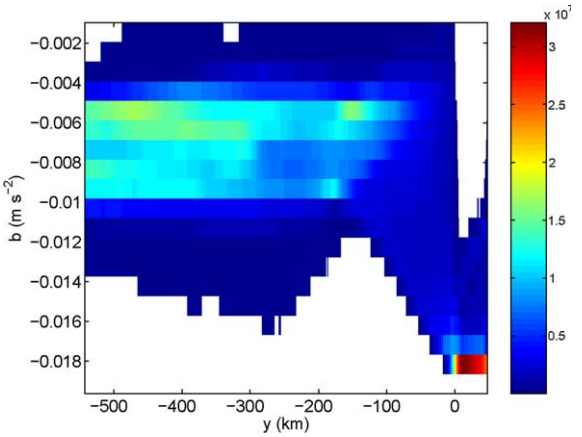

Fig. 8. The total tracer τ as a function of cross-slope distance and buoyancy class, time-averaged over the latter half of the simulation, for Case 4 (*no f*), simulated at a resolution of $\Delta x \times \Delta z = 500\ \mathrm{m} \times 30\ \mathrm{m}$ with the non-hydrostatic MITgcm.

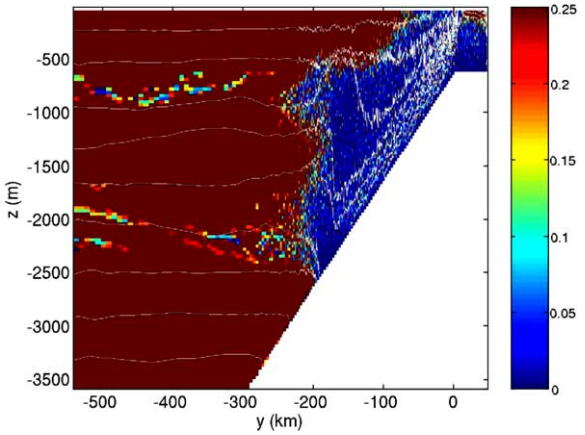

Fig. 9. The instantaneous local gradient Richardson number defined by $Ri = (\partial b/\partial z)/(\partial U/\partial z)^2$ in a vertical plane at $x = 0$ and a time of $t = 13$ days, for Case 4 (*no f*), simulated at a resolution of $\Delta x \times \Delta z = 500\ \text{m} \times 30\ \text{m}$ with the non-hydrostatic MITgcm.

it reaches neutral buoyancy, when Richardson numbers rapidly increase to >0.25. Hence the region of entrainment and diapycnal mixing, from -150 km $< y < 0$ km coincides with the region of low *Ri*, as expected if shear instability is the dominant cause of both mixing and entrainment.

3.3. Case 6 (no N^2): with rotation, without ambient stratification

Finally we describe the features of a simulation with rotation, but without stratification. Qualitatively, as seen in Fig. 10, the flow resembles that of *Ref*, the dense water is deflected along the slope, and the flow is dominated by eddies. The overflow fluid descends further down the slope

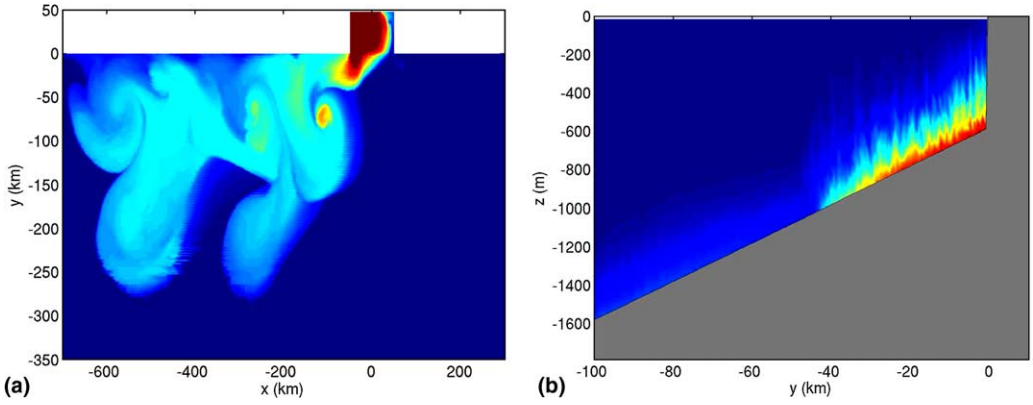

Fig. 10. Passive tracer concentration τ at a time 13 days after the initiation of the dense inflow, for Case 6 (*no* N^2), at a resolution of $\Delta x \times \Delta z = 500\ \text{m} \times 30\ \text{m}$, simulated by the non-hydrostatic MITgcm: (a) τ just above the topography, as a function of horizontal distance and (b) τ in a vertical slice at $x = -50$ km, near the inflow. τ has a value of zero in the ambient fluid, and $\tau = 1$ in the inflow.

than in *Ref*, and much of this is in the form of thin, dilute sheets, in which Ekman flow probably plays an important role. Again, most of the dilution of tracer, and hence mixing with ambient fluid, takes place near the inflow where small-scale mixing is found (Fig. 10b). Dilution is even more rapid than in *Ref*, and the final tracer concentration weaker. The lack of ambient stratification means that the dense fluid never reaches a neutral buoyancy level, and hence never detrains from the slope into the interior, hence the greater role for Ekman flow. As the dense water descends the buoyancy anomaly does not diminish as in the ambient stratification of *Ref*, and so the conversion of potential energy to kinetic energy is maintained.

Fig. 11(a) shows the instantaneous along-slope transport. In comparison with *Ref*, the transport shows negligible increase in the along-slope direction after the corner region. Entrainment deduced from this transport (Fig. 11(b)) therefore drops rapidly to zero away from the inlet. The average entrainment in the corner region itself is 7.5×10^{-4}, comparable to that of *Ref*.

The total tracer as a function of along-slope distance and buoyancy (Fig. 12) shows that, like *Ref*, the tracer maximum moves rapidly from the buoyancy of the inflow $b < -0.018$ m/s^2 to a value of $-0.006 < b < -0.004$ m/s^2, a lighter buoyancy level than in *Ref*. Hence despite the continued buoyancy difference between overflow water and ambient fluid, all diapycnal mixing ceases after about $x = -150$ km. In comparison with *Ref*, entrainment and diapycnal mixing occur over an even shorter distance.

To summarize these three high-resolution calculations: in both rotating cases the flow is predominantly along-slope, as would be expected following geostrophic adjustment on the slope, the entrainment and mixing occur close to the inflow (before the flow has adjusted to move along the slope), and the region of the flow dominated by eddies does not appear to be the location of significant entrainment. The location of mixing is probably due to the sudden change in bottom slope encountered as the dense fluid leaves the embayment, but the role of the embayment geometry cannot be ruled out from the current simulations. The eddies may cause the entrainment

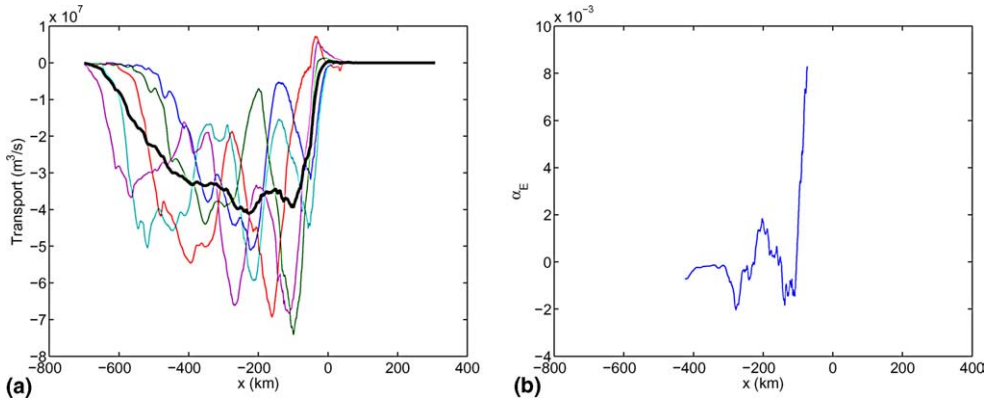

Fig. 11. For Case 6 (*no* N^2), simulated at a resolution of $\Delta x \times \Delta z = 500$ m $\times$ 30 m with the non-hydrostatic MITgcm: (a) the total along-slope transport in the overflow fluid (identified by $\tau > 0.01$), as a function of along-slope distance (with the center of the inlet at $x = 0$). Several instantaneous values of transport are shown (at time intervals of 1.16 days), with the mean of these values overlain as a thick solid line and (b) The entrainment coefficient diagnosed from the time-mean transport, for the region west of the inlet entrance at $x = -50$ km, as a function of along-slope distance.

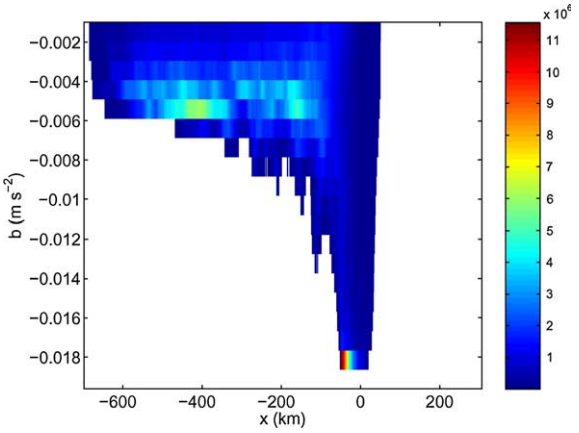

Fig. 12. The total tracer τ as a function of along-slope distance and buoyancy class, time-averaged over the latter half of the simulation, for Case 6 (*no* N^2), simulated at a resolution of $\Delta x \times \Delta z = 500\ \mathrm{m} \times 30\ \mathrm{m}$ with the non-hydrostatic MITgcm.

to cease as the flow becomes more barotropic through the development of the eddies. (Girton and Legg (in preparation) examines the role of eddies in modifying entrainment in greater detail.) In contrast, in the non-rotating case, all flow is directed down the slope, and low Richardson numbers, with associated diapycnal mixing and entrainment, are associated with the entire plume up until neutral buoyancy is reached. In both rotating and non-rotating cases, the entrainment and diapycnal mixing are found in the same location (along-isopycnal entrainment is not significant), and this location coincides with low Richardson numbers, and finite vertical buoyancy stratification.

In all three cases, the bulk Richardson number near the top of the slope is between 0.4 and 0.5, from which the Ellison–Turner formula would predict an entrainment coefficient of between 8×10^{-3} and 4×10^{-2}. The entrainment coefficient at the top of the slope in *no f* lies within this range, but that in the two rotating calculations is considerably smaller. Recent laboratory studies suggest that rotation probably modifies the entrainment process by modifying the plume velocities (Mathew Wells, private communication); this geostrophic adjustment of the plume is resolved by the numerical simulations, and occurs within the corner region where entrainment was diagnosed.

Baines (2001) and Baines (2002) show that in the laboratory, two different regimes may be identified for non-rotating plumes in a stratified environment. When the "buoyancy parameter" $B = QN^3/(\Delta b_0)^2$ is large and bottom drag is small, the entraining plume model dominates, and the plume overshoots its neutral buoyancy level. When B is small, and bottom drag is large, detrainment occurs over most of the plume's length and there is no overshoot. The separation between the two regimes is given by (Baines, submitted)

$$C_\mathrm{d} + \alpha_\mathrm{E} - 0.2B^{0.4} \sin\theta = 0 \tag{16}$$

Our parameters appear to lie in the regime where Baines (submitted) would suggest detrainment should dominate. However, we observe an overshoot beyond the neutral buoyancy level, and only a small amount of detrainment prior to reaching neutral buoyancy. These discrepancies suggest that the model does not correctly capture the detrainment physics at this resolution.

4. Comparison with coarser resolution simulations

We now compare these high-resolution calculations with identical calculations run at lower resolution, as well as three other cases, run at the lower resolutions only. Fig. 13 shows the equivalent of Fig. 2(a) for *Ref* at three lower resolutions for the z-coordinate model and at two lower resolutions for the isopycnal coordinate model. In the z-coordinate calculations, at 2.5 km resolution eddies are present, but no small-scale structure is even partially resolved. At 10 km resolution, eddies are absent, and the flow looks more similar to the laminar regime found at higher Ekman numbers in the laboratory experiments of Cenedese et al. (2004). At 50 km resolution even the overall plume structure is poorly resolved and the plume descends much less down the slope. The 10 km isopycnal coordinate calculation includes more eddy structure than the 10 km z-coordinate calculation and does not descend so far down the slope (both are consistent with the much smaller vertical viscosity in the isopycnal model, as discussed below). The 50 km isopycnal coordinate calculation resembles a coarse-grained version of the 10 km calculation, and hence less qualitative changes are introduced by the coarser resolution than for the z-coordinate model. (Ezer and Mellor (2004) and Ezer (2005) show that terrain-following models are also relatively insensitive to resolution.)

For quantitative comparison of resolution dependence we focus on three key parameters: the average entrainment in the corner region (since we have seen this is where most of the entrainment occurs in the rotating cases), the final buoyancy where the maximum tracer is found as a marker of diapycnal mixing, and the descent of the overflow water down the slope.

Fig. 14 shows the average entrainment in the corner region as a function of resolution for the six different cases. We do not show the entrainment for the 50 km resolution z-coordinate simulations, since the poorly developed sluggish flow does not lead to a well-defined increase in transport on the slope, and in fact there is sometimes detrainment as overflow fluid spreads in the opposite direction. For the z-coordinate calculations we note that the entrainment coefficient is uniformly smaller at coarser resolution, but that different cases show different sensitivity to different resolutions. Whereas at a resolution of 2.5 km, all the rotating cases have entrainment coefficients which are quite close in value, at 10 km resolution the entrainment in $0.1\Delta b_0$ is reduced most strongly, that in $0.5\Delta b_0$ and 0.5 *slope* less strongly, and that in *Ref* and *no* N^2 least of all. We can relate this sensitivity to the parameter Γ or to the deformation radius: $0.1\Delta b_0$ has the smallest value of Γ, $0.5\Delta b_0$ and 0.5 *slope* intermediate values, and *Ref* and *no* N^2 the largest values. Physically perhaps cases with smaller deformation radii are affected more by the change in resolution. The decrease in entrainment as Δx increases may in part be due to a decrease in the dense flow velocity at coarser resolution, a trend which is in part probably determined by the increased viscosity at coarser resolution. The calculations with the isopycnal model all show less dependence of entrainment on model parameters at 10 km resolution than for the z-coordinate calculations. Entrainment is somewhat higher, and in fact higher than the z-coordinate calculations at 500 m resolution except for Case 4 (non-rotating). Changing resolution from 10 km to 50 km produces a small decrease in entrainment in the isopycnal model, probably attributable to decreases in the resolved velocity from which entrainment is calculated using the Ellison–Turner parameterization.

Fig. 15 shows the final buoyancy b_f of the overflow, as a function of resolution for each of the six different cases. The location of the overflow water in buoyancy space as a function of along-slope distance (or cross-slope distance for the non-rotating case) is defined as:

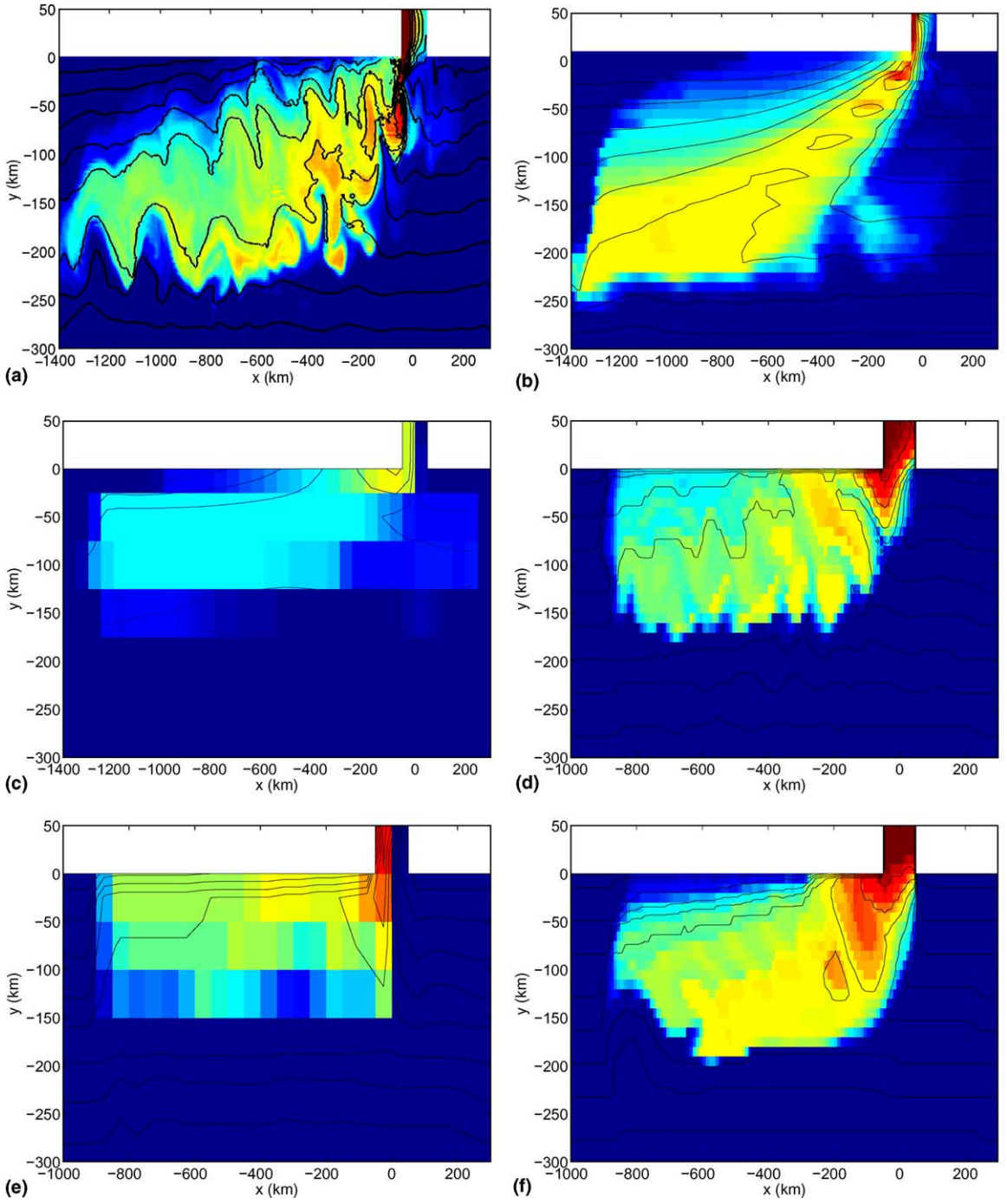

Fig. 13. Passive tracer concentration τ just above the topography, as a function of horizontal distance, with buoyancy contours overlain, for Case 1 (*Ref*) simulations at different resolutions, and using different model types: (a) $\Delta x \times \Delta z = 2.5\,\mathrm{km} \times 60\,\mathrm{m}$, MITgcm; (b) $\Delta x \times \Delta z = 10\,\mathrm{km} \times 144\,\mathrm{m}$, MITgcm; (c) $\Delta x \times \Delta z = 50\,\mathrm{km} \times 144\,\mathrm{m}$, MITgcm; (d) $\Delta x \times \Delta b = 10\,\mathrm{km} \times 25$ layers, HIM; (e) $\Delta x \times \Delta b = 50\,\mathrm{km} \times 25$ layers, HIM; (f) as for (d) but with increased ν_v.

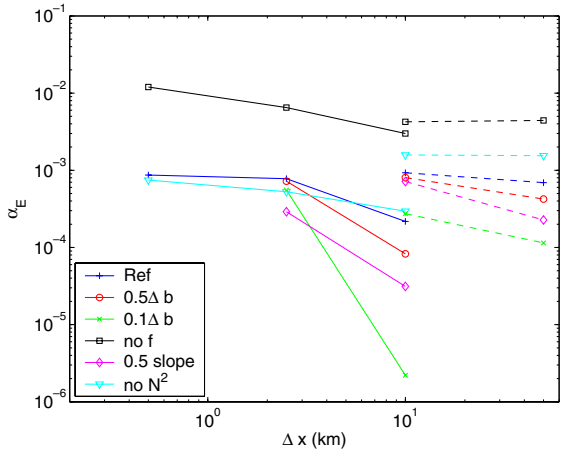

Fig. 14. The average entrainment in the corner region defined by -50 km $< x < 50$ km, -50 km $< y < 0$ km, shown as a function of resolution for all six cases. z-coordinate calculations are shown with solid lines, isopycnal coordinate calculations are shown with dashed lines.

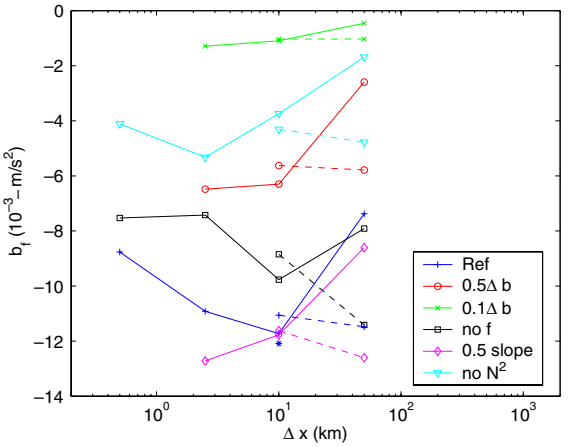

Fig. 15. The final buoyancy of the overflow b_f, following mixing and entrainment, shown as a function of resolution for each of the six different cases. z-coordinate calculations are shown with solid lines, isopycnal coordinate calculations are shown with dashed lines. The asterisk shows the result for the 10 km horizontal resolution isopycnal calculation with increased vertical viscosity.

$$b(x) = \frac{\int b(x,y,z)\tau(x,y,z)\,\mathrm{d}y\,\mathrm{d}z}{\int \tau(x,y,z)\,\mathrm{d}y\,\mathrm{d}z} \tag{17}$$

We find the time-average of this path in buoyancy space (once statistical steady-state has been reached) and then average over the distance over which $b(x)$ is approximately constant with distance to obtain b_f.

Fig. 15 shows that the trend of final buoyancy b_f with resolution is not monotonic. All cases show an increase in final buoyancy at the coarsest resolution of 50 km, consistent with excessive

spurious mixing expected when $\Delta x > H/\tan\theta$. However, those cases run at 500 m resolution also show an increased final buoyancy at this resolution, as compared to the intermediate resolution cases. We suspect that if $0.5\Delta b_0$, $0.1\Delta b_0$ and 0.5 *slope* were run at 500 m, we would find that they also have a minimum in final buoyancy (and hence a minimum in diapycnal mixing) at the intermediate resolutions.

At a resolution of 10 km the final buoyancy seen in the isopycnal and z-coordinate models is very similar. However, on changing resolution to 50 km, the isopycnal model shows a small decrease in final buoyancy (indicating less mixing), unlike the large increase in mixing seen in the z-coordinate 50 km calculations.

This very different response to changing resolutions reflects the way that the vigorous mixing is manifest in the two models. In the z-coordinate calculations, the mixing is due to partially resolved shear-driven overturning at the highest resolutions and unconstrained numerical mixing at the lowest resolutions. In the isopycnal model, the entrainment is solely due to the parameterized mixing. As a deliberate part of the parameterization, this mixing controls the shears that would drive mixing were they present in the higher resolution z-coordinate simulations. The dominant source of energy to drive mixing is the horizontally broad (but vertically concentrated) shears at the top of the plume, and these broad shears are similar at the leading order in both the 10 km and 50 km isopycnal calculations. If spurious numerical mixing were greatly reduced (which is a formidable challenge) and a deliberate parameterization of unresolved mixing were introduced, it is very likely that the z-coordinate model would have a similarly weak dependence on resolution.

Finally Fig. 16 shows the mean path of the plume for each of the five rotating cases as a function of resolution. The mean path is defined by

$$Y(x) = \frac{\int y\tau(x,y,z)\,\mathrm{d}y\,\mathrm{d}z}{\int \tau(x,y,z)\,\mathrm{d}y\,\mathrm{d}z} \tag{18}$$

and is time-averaged once a statistically steady-state is reached. For the z-coordinate model we note the following trend in all cases: for $\Delta x = 2.5$ km and $\Delta x = 10$ km, the path taken down the slope is initially very similar; however, for $\Delta x = 2.5$ km the path changes and aligns itself with the along-slope direction closer to the inlet. The least descent is seen for $\Delta x = 500$ m, consistent with the more rapid mixing and small vertical viscosity in these calculations. For $\Delta x = 500$ km the path is less steep than for the intermediate resolution cases, but not aligned along slope as soon as for $\Delta x = 500$ m. The steepness of descent therefore follows the same trend as the changes in buoyancy, as one would expect, with less mixing associated with greater down-slope momentum. Interestingly, the introduction of eddies, which occurs as Δx is reduced from 10 km to 2.5 km makes little difference to the average path down the slope, perhaps because at $\Delta x = 10$ km the higher vertical friction compensates for the absence of eddies. By comparison, the isopycnal model shows a path much more aligned with the along-slope direction for both $\Delta x = 10$ km and $\Delta x = 50$ km, consistent with the snapshots shown in Fig. 13. A possible cause might be the much smaller vertical viscosity in the isopycnal model.

To test the effects of the much larger vertical viscosity in the z-coordinate model, an additional 10 km resolution isopycnal model simulation of the reference case was done with the much larger vertical viscosity of the z-coordinate model ($0.5\ \mathrm{m^2\ s^{-1}}$ vs. $10^{-4}\ \mathrm{m^2\ s^{-1}}$). The eddies are strongly suppressed in this viscous simulation (Fig. 13f). Consistent with the viscous suppression of the

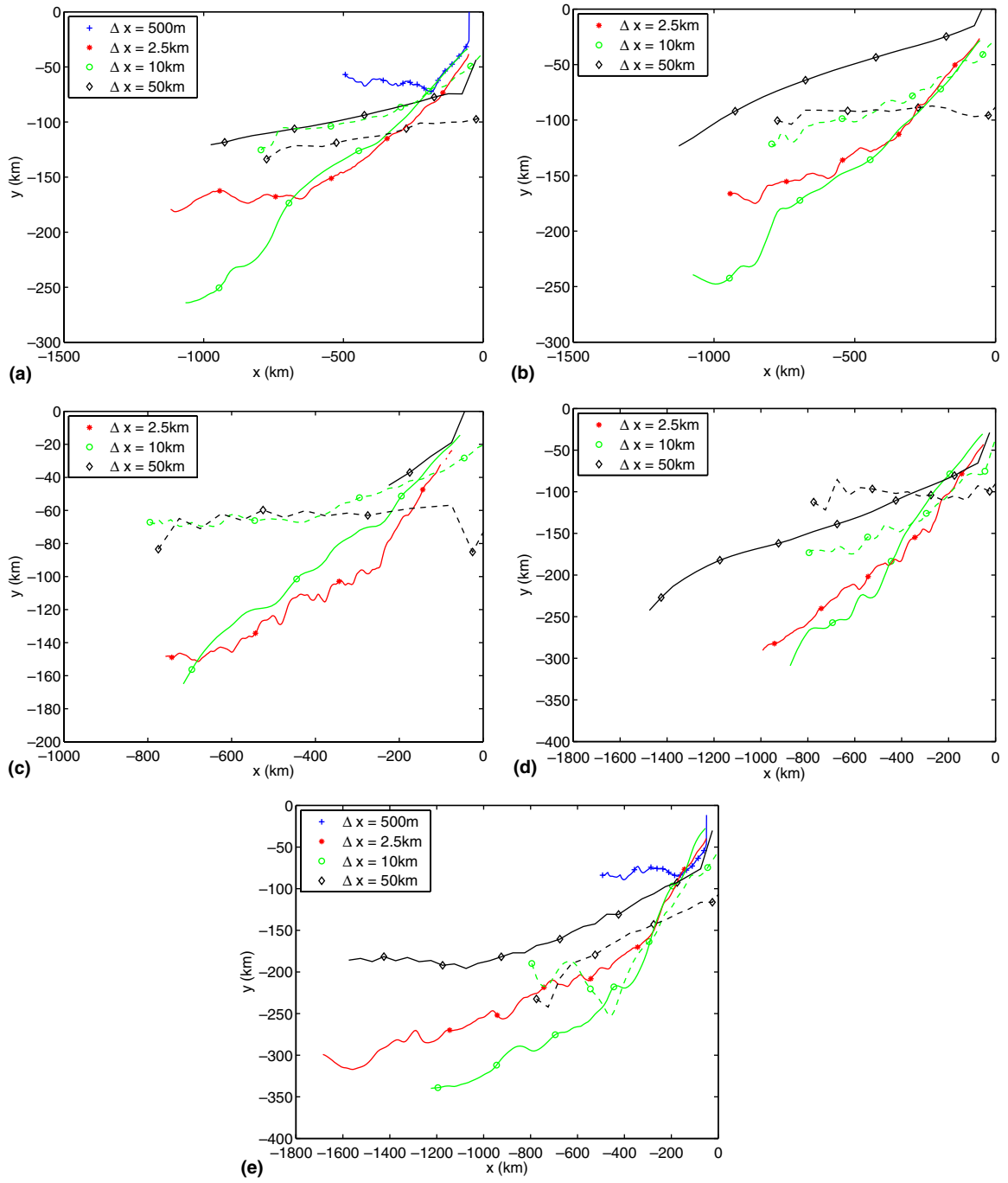

Fig. 16. The mean path of the overflow water, as determined from the passive tracer center of gravity, as a function of resolution for each of the five different rotating cases: (a) Case 1 (*Ref*); (b) Case 2 (0.5Δ*b*); (c) Case 3 (0.1Δ*b*); (d) Case 5 (0.5 *slope*); (e) Case 6 (*no* N^2). Five or six different calculations are shown for each case: with *z*-coordinate and isopycnal calculations shown by solid and dashed lines, respectively.

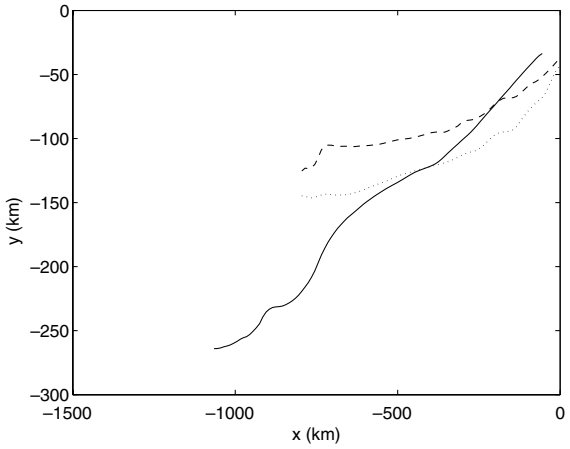

Fig. 17. The mean path of the overflow water, as determined from the passive tracer center of gravity, as a function of vertical viscosity and model type for Case 1 (*Ref*) at 10 km horizontal resolution: z-coordinate, $\nu_v = 5 \times 10^{-1}$ m^2/s (solid); isopycnal coordinate, $\nu_v = 10^{-4}$ m^2/s (dashed); isopycnal coordinate, $\nu_v = 5 \times 10^{-1}$ m^2/s (dotted).

shears that drive the parameterized mixing, the final plume density is higher (and in fact is now higher than the 10 km z-coordinate model) (Fig. 15). The path of the plume in the viscous case reaches about 40 km further down the slope, accounting for most of the difference in the paths between the two models (Fig. 17). This is consistent with an increase in down-slope bottom Ekman transport with higher viscosity (as seen also in Ezer (2005)). There are other significant differences between the two models, especially the different formulations of horizontal viscosity and the differing barotropic circulations that evolve with the presence or lack of a true open boundary condition at the outflows. But despite these differences, it is significant that there is an intermediate resolution regime, predictable from previous theory, where the two models behave rather similarly. We are confident that the highly resolved non-hydrostatic simulations will provide invaluable guidance in refining the parameterizations for use in this regime within large-scale ocean simulations.

5. Discussion and conclusions

We have described a series of simulations, at four different resolutions, with six different combinations of physical parameters, and using two different numerical model types, designed to investigate the sensitivity of overflow simulations to model resolution and type, over a range of physical regimes. We have focused on the entrainment and diapycnal mixing which takes place in an overflow. We find that the net amount of diapycnal mixing which takes place is strongly dependent on model resolution for the z-coordinate model: mixing is increased at higher resolutions (when non-hydrostatic mixing processes are permitted) and at coarse resolutions (when the mixing is spurious, and due to the inability of the model to move fluid down the slope without invoking convective adjustment). Current z-coordinate climate models are in the coarse resolution limit of our simulations, and hence effort is being devoted to preventing this spurious mixing in

overflow regions, by implementing schemes designed to move dense fluid more efficiently down the slope. However, as resolution increases, future models will likely move into the regime where mixing is less than in the high resolution simulations (which in the absence of infinitely high resolution calculations we are forced to use as our best guess at the truth). Hence, future z-coordinate climate models may ultimately be in a position to adopt bottom boundary mixing parameterization schemes as a means of representing the mixing in gravity currents, such as currently practiced in sigma coordinate models, which use turbulence closure models such as Mellor and Yamada (1982).

For the isopycnal coordinate model, we find that in comparison with the non-hydrostatic simulations, entrainment is slightly greater at 10 km resolution, while the diapycnal mixing is about the same (*no* N^2) or somewhat less (*Ref*). Both entrainment and mixing decrease as resolution coarsens, as less extrema in shear are resolved. As all of the mixing and much of the entrainment is entirely due to the Richardson number-based parameterization, this resolution dependence might be further reduced by adjusting the parameterization to take into account how much of the shear spectrum is resolved.

We can compare our results with the sigma-coordinate calculations of Ezer and Mellor (2004), which use the same configuration as our *Ref*. Their calculation Sl uses a horizontal resolution of 10 km with horizontal viscosity of 5×10^1 m^2/s, as for our z-coordinate 10 km calculations. The sigma-coordinate calculation shows slightly more eddy activity than the our z-coordinate calculation at similar resolution, while following a less steep descent down the slope. These differences may again be due to the difference in vertical viscosity (supplied by the Mellor–Yamada scheme in the sigma model). The sigma-coordinate calculation is qualitatively similar to the isopycnal coordinate calculation at the same resolution. Like the isopycnal coordinate simulations, sigma coordinate simulations show less resolution dependence than z-coordinate simulations. Note that our 10 km and 2.5 km z-coordinate calculations bear little resemblance to the z-coordinate calculations of Ezer and Mellor (2004) at the same resolution (which produced much less descent than the sigma coordinate calculations, and much more mixing) primarily because the MITgcm employs the more accurate partial step topography, rather than the full step topography used by Ezer and Mellor (2004). Differences may also be due to the use of the Mellor–Yamada mixing scheme by Ezer and Mellor (2004).

We may also compare our results with measurements from the Denmark Straits Overflow. Over the 200 km downstream of the sill where measurements were made, Girton and Sanford (2003) found a rate of descent of 6 m/km, somewhat steeper than seen in any of our rotating simulations (*no* N^2 having the steepest rate of descent at 4.5 m/km, deduced from Fig. 16); however the topographic slope is somewhat steeper in the Denmark Straits region than in our configuration. The downstream change in plume density seen in the Denmark Straits Overflow (0.1 kg/m^3) is substantially smaller than in our *Ref* and *no* N^2 simulations (from Fig. 15), but lies between that seen in $0.5\Delta b_0$ and $0.1\Delta b_0$, which is expected since the initial buoyancy anomaly in the Denmark Straits is between those two values. Finally the entrainment velocity diagnosed in the Denmark Straits overflow lies between 6×10^{-5} m/s and 8×10^{-4} m/s. This is less than the entrainment velocity diagnosed in our *Ref* and *no* N^2 calculations, but greater than that in the 2.5 km resolution $0.5\Delta b_0$ and $0.1\Delta b_0$ calculations (entrainment velocities are not shown here, but are an intermediate step in the calculation of the entrainment coefficient). Given the tendency of the z-coordinate model to underestimate entrainment at lower resolution, it is likely that a simulation with the

appropriate initial buoyancy anomaly at high resolution would generate entrainment of about the same order as seen in the observations. While we cannot say anything more specific about the ability of the model to simulate real flows without employing more realistic topography, stratification and inflow forcing, it appears that the model has the capability to be used at high resolution to give estimates of entrainment of the right order of magnitude. Future work, e.g. as part of the Gravity Current Entrainment Climate Process Team, will examine the correspondence between realistic simulations and observations more closely.

An important result for models at intermediate resolutions (i.e. where $h/\tan\alpha < \Delta x$) is the controlling effect of vertical viscosity, in both determining whether eddies are possible, and enhancing downslope flow (although entrainment and mixing are less sensitive to the vertical viscosity). Since the z-coordinate model requires larger vertical viscosity for numerical reasons compared to the isopycnal model, the solutions at $\Delta x = 10$ km are qualitatively quite different.

Acknowledgment

The authors would like to express their thanks to Hartmut Peters and other members of the Gravity Current Entrainment Climate Process Team for useful and stimulating discussions. Comments from Claudia Cenedese, Harper Simmons, Steve Griffies and two anonymous reviewers helped to improve the manuscript.

Appendix A. Bottom mixing parameterization

Here we describe a new parameterization of bottom boundary mixing for isopycnal models, employed in all the isopycnal simulations in this study. Isopycnal models have previously used the shear Richardson number to parameterize diapycnal mixing. The source of this energy is the resolved shear, and it has proven capable of capturing many aspects of mixing in the interfacial layer at the top of dense plumes. Plumes, however, also tend to have well-mixed boundary layers (Peters et al., in press), and the previous parameterizations for isopycnal models (Hallberg, 2000) have not included the vigorous mixing that occurs within the homogeneous bottom layer.

The well-mixed bottom layer is a region of three-dimensional turbulence. Although the shear Richardson numbers can be locally quite small within this bottom layer, the source of turbulent energy is as likely to be emanating from interactions between the mean flow and the boundary as it is from local velocity shears.

In this paper, we introduce a parameterization of bottom boundary layer mixing to complement the shear-Richardson number parameterization that applies in the interfacial layer at the top of the plume. It is assumed that the source of energy to drive mixing is the energy extracted from the mean flow by the bottom drag. With a quadratic bottom drag, energy is extracted at a rate

$$E_{\mathrm{BBL}} = \rho_0 c_D \mid u_{\mathrm{BBL}} \mid u_{\mathrm{BBL}} \cdot u_{\mathrm{BBL}} = \rho_0 u^{*3} \tag{A.1}$$

It is assumed that a substantial portion of this energy is dissipated within the bottom boundary layer, and that there is an assumed efficiency γ with which this extracted energy drives diapycnal

mixing. (This relationship between turbulent dissipation and diapycnal mixing is essentially the well known Osborn-Cox relationship (Osborn and Cox, 1972).) Direct measurements of turbulent mixing in stratified fluids indicate that the efficiency with which turbulent dissipation translates into diapycnal mixing is of order 20% (Ivey and Imberger, 1991), so this is a reasonable value to choose for γ, although γ must be considered the tunable parameter of this parameterization. The parameterization here is to apply this energy to the deepest resolved stratification, which will be within the bottom boundary layer or at the top of the bottom boundary layer. In addition, surface mixed layer parameterizations have found that the agreement with observations is improved if a rotationally induced decay of $\exp(-zf/ku^*)$ is used, where $\kappa = 0.4$ is the von Karman constant (Oberhuber, 1993) and z is the distance between where the turbulence is generated and where its mixing is realized.

In an isopycnal model, diapycnal mixing occurs through a layer entraining its neighbors (McDougall and Dewar, 1998). The bottommost massive layer cannot entrain from massless layers below, and it cannot entrain solely from layers above and still retain its prescribed density, so the bottom mixing is expressed as entrainment both from above and below by the second massive layer from the bottom. Using the relationship between work and diapycnal mixing the diapycnal diffusivity in the second layer from the bottom is set to be

$$\kappa_{B-1} = \max\left(\kappa_{\text{Background}}, \kappa_{Ri}, \frac{\gamma E_{\text{BBL}} \exp[-(h_B + h_{B-1}/2)f/ku^*]}{g\Delta\rho_{B-1}}\right) \tag{A.2}$$

where the subscripts B and $B-1$ refer to the bottom layer and the next layer up, respectively, and $\Delta\rho_{B-1}$ is the density jump across second layer from the bottom (see Hallberg (2000) for an exact definition when the density differences between layers are not uniform). If mixing due to the resolved shear Richardson numbers or the background diffusivity would be more intense, this bottom source of mixing is simply omitted in this prescription.

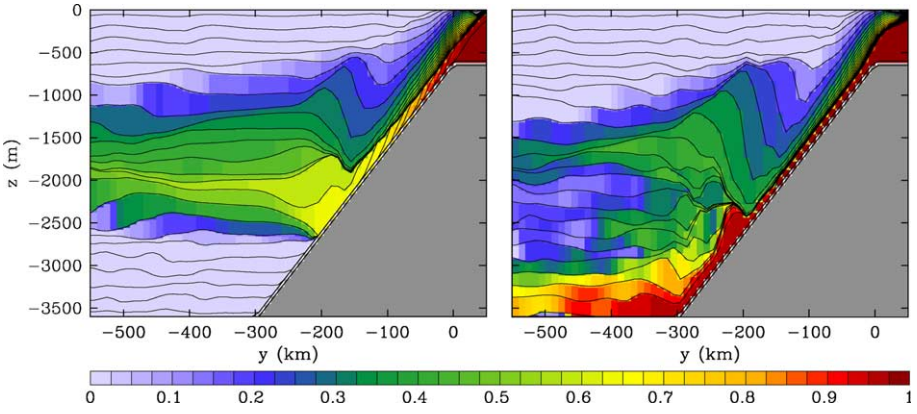

Fig. A.1. Passive tracer concentration τ in a meridional slice through the middle of the inflow at time 12.5 days after the initiation of the dense inflow, for the non-rotating Case 4 (*no f*), in the isopycnal model at a resolution of 10 km. This figure is comparable to Fig. 6a. In (a), the bottom-drag induced mixing parameterization is included with an efficiency of 20%; this is the setting used throughout the paper. In (b), the bottom-drag induced mixing is omitted (or equivalently has an efficiency of 0). Without the bottom mixing, nearly undiluted overflow water flows into the abyss in a highly viscous but adiabatic bottom boundary layer.

This additional bottom source of mixing has a dramatic effect on the simulations, as shown in Fig. A.1. Without the bottom mixing, a thin sheet of dense and tracer laden fluid creeps down the slope within a viscous bottom boundary layer. While this creeping flow may be reasonable in low Reynolds number laboratory flows, in an oceanographic context the near-bottom viscosities that support it are much higher than molecular values, and the bottom boundary layer should be turbulent. The added bottom mixing greatly reduces the propensity for a secondary, thin, dense plume, essentially by providing a diffusivity that is more commensurate with the expected turbulence in the bottom boundary layer.

This new parameterization of bottom-layer mixing is based upon a plausible conversion of some of the energy extracted from the resolved flow by bottom drag into turbulent kinetic energy that supports the diapycnal mixing. Although it dramatically improves the simulations presented here, it should be considered a qualitatively reasonable placeholder for future parameterizations that will be developed by studying high-resolution simulations and observations of oceanic bottom boundary layers.

References

Adcroft, A., Hill, C., Marshall, J., 1997. Represention of Topography by Shaved Cells in a Height Coordinate Ocean Model. Mon. Wea. Rev. 125, 2293–2315.

Adcroft, A., Hill, C., Marshall, J., 1999. A new treatment of the Coriolis terms in C-grid models at both high and low resolutions. Mon. Wea. Rev. 127, 1928–1936.

Baines, P., 2001. Mixing in flows down gentle slopes into stratified environments. J. Fluid. Mech. 443, 237–270.

Baines, P., 2002. Two-dimensional plumes in stratified environments. J. Fluid. Mech. 471, 315–337.

Baines, P.G., submitted. Regimes for the flow of dense fluid down slopes into stratified environments. J. Fluid. Mech.

Beckmann, A., Doscher, R., 1997. A method for improved representation of dense water spreading over topography in geopotential-coordinate models. J. Phys. Oceanogr. 27, 581–591.

Campin, J.-M., Goose, H., 1999. Parameterization of density-driven downslope flow for a coarse-resolution ocean model in *z*-coordinate. Tellus 51, 412–430.

Cenedese, C., Whitehead, J.A., Ascarelli, T., Ohiwa, M., 2004. A dense current flowing down a sloping bottom in a rotating fluid. J. Phys. Oceanogr. 34, 188–203.

Dickson, R., Brown, J., 1994. The production of North-Atlantic deep water-sources, rates and pathways. J. Geophys. Res. 99, 12139–12341.

Easter, R., 1993. Two modified versions of Bott's positive-definite numerical advection scheme. Mon. Wea. Rev. 121, 297–304.

Ellison, T., Turner, J., 1959. Turbulent entrainment in stratified flows. J. Fluid. Mech. 6, 423–448.

Ezer, T., Arango, H., Shchepetkin, A., 2002. Developments in terrain-following ocean models: intercomparisons of numerical aspects. Ocean Model 4, 249–267.

Ezer, T., Mellor, G., 2004. A generalized coordinate ocean model and a comparison of the bottom boundary layer dynamics in terrain-following and *z*-level grids. Ocean Model. 6, 379–403.

Ezer, T., 2005. Turbulent entrainment, diapycnal mixing and transport in three-dimensional bottom gravity current simulations using the Mellor-Yamada turbulence scheme. Ocean Model. 9, 151–168.

Girton, J., Legg, S., in preparation. Mechanisms of entrainment and descent in rotating gravity currents. J. Phys. Oceanogr.

Girton, J., Sanford, T., 2003. Descent and modification of the overflow plume in the Denmark Strait. J. Phys. Oceanogr. 33, 1351–1364.

Gordon, A., Visbeck, M., Huber, B., 1998. Export of Weddell Sea deep and bottom water. J. Geophys. Res. 106, 9005–9017.

Griffies, S., Boning, C., Bryan, F., Chassignet, E., Gerdes, R., Hasumi, H., Hirst, A., Treguier, A., Webb, D., 2000. Developments in ocean climate modeling. Ocean Model. 2, 123–192.

Griffies, S.M., Hallberg, R., 2000. Biharmonic friction with a Smagorinsky-like viscosity for use in large-scale eddy permitting ocean models. Mon. Wea. Rev. 128, 2935–2946.

Haidvogel, D., Arango, H., Kedstrom, K., Beckmann, A., Malanotte-Rizzoli, P., Shchepetkin, A., 2000. Model evaluation experiments in the North Atlantic Basin: simulations in nonlinear terrain-following coordinates. Dyn. Atmos. Oceans 32 (3–4), 239–281.

Hallberg, R., 1997. Stable split time stepping schemes for large-scale ocean modelling. JCP 135, 54–65.

Hallberg, R., 2000. Time integration of diapycnal diffusion and richardson number—dependent mixing in isopycnal coordinate ocean models. Mon. Wea. Rev. 128, 1402–1419.

Hallberg, R., Rhines, P., 1996. Buoyancy-driven Circulation in an Ocean Basin with Isopycnals Intersecting the Sloping Boundary. J. Phys. Oceanogr. 26, 913–940.

Haney, R., 1991. On the pressure-gradient force over step topography in sigma coordinate ocean models. J. Phys. Oceanogr. 21 (4), 610–619.

Ivey, G., Imberger, J., 1991. On the nature of turbulence in a stratified fluid. Part I: The energetics of mixing. J. Phys. Oceanogr. 25, 650–658.

Jiang, L., Garwood, R., 1996. Three-dimensional simulations of overflows on continental slopes. J. Phys. Oceanogr. 26, 1214–1233.

Killworth, P., Edwards, N.R., 1999. A turbulent bottom boundary layer code for use in numerical ocean models. J. Phys. Oceanogr. 29, 1221–1238.

Lane-Serff, G., Baines, P., 1998. Eddy formation by dense flows on slopes in a rotating fluid. J. Fluid. Mech. 363, 229–252.

Lane-Serff, G., Baines, P., 2000. Eddy formation by overflows in stratified water. J. Phys. Oceanogr. 30, 327–337.

Marshall, J., Adcroft, A., Hill, C., Perelman, L., Heisey, C., 1997a. A finite-volume, incompressible Navier–Stokes model for studies of the ocean on parallel computers. J. Geophys. Res. 102 (C3), 5753–5766.

Marshall, J., Hill, C., Perelman, L., Adcroft, A., 1997b. Hydrostatic, quasi-hydrostatic, and nonhydrostatic ocean modeling. J. Geophys. Res. 102 (C3), 5733–5752.

McDougall, T., Dewar, W., 1998. Vertical Mixing and Cabbeling in Layered Models. J. Phys. Oceanogr. 28, 1458–1480.

Mellor, G., Yamada, T., 1982. Development of a turbulent closure model for geophysical fluid problems. Rev. Geophys. 20, 851–875.

Oberhuber, J., 1993. Simulation of the Atlantic circulation with a coupled sea ice-mixed layer-isopycnal general circulation model. Part I: Model Description. J. Phys. Oceanogr. 23, 808–829.

Orlanski, I., 1976. A simple boundary condition for unbounded hyperbolic flows. J. Comp. Phys. 21, 251–269.

Osborn, T., Cox, C., 1972. Oceanic fine structure. Geophys. Fluid Dyn. 3, 321–335.

Papadakis, M., Chassignet, E., Hallberg, R., 2003. Numerical simulations of the Mediterranean sea outflow: impact of the entrainment parameterization in an isopycnic coordinate ocean model. Ocean Model. 5, 325–356.

Peters, H., Johns, W., Bower, A., Fratantoni, D., in press. Mixing and entrainment in the Red Sea outflow plume. Part I. Plume structure. J. Phys. Oceanogr. 35.

Pietrzak, J., 1998. The use of TVD Limiters for forward-in-time upstream-biased advection schemes in ocean modeling. Mon. Wea. Rev. 126, 812–830.

Price, J., Baringer, M., 1994. Overflows and deep water production by marginal seas. Progress in Oceanogr. 33, 161–200.

Price, J., Baringer, M., Lueck, R., Johnson, G., Ambar, L., Parrilla, G., Cantos, A., Kennelly, M., Sanford, T., 1993. Mediterranean outflow mixing and dynamics. Science 259, 1277–1282.

Shchepetkin, A., McWilliams, J., 2003. A method for computing horizontal pressure gradient force in an oceanic model with nonaligned vertical coordinate. J. Geophys. Res., 108.

Song, Y., Chao, Y., 2000. An embedded bottom boundary layer formulation for z-coordinate ocean models. J. Ocean Atmos. Tech. 17, 546–560.

Turner, J., 1986. Turbulent entrainment: the development of the entrainment assumption and its application to geophysical flows. J. Fluid. Mech. 173, 431–471.

Willebrand, J., Barnier, B., Boning, C., Dieterich, C., Killworth, P., Provost, C.L., Jia, Y., Molines, J.-M., New, A., 2001. Circulation characteristics in three eddy-permitting models of the North Atlantic. Progress in Oceanography 48, 123–161.

Winton, M., Hallberg, R., Gnanadesikan, A., 1998. Simulation of density-driven frictional downslope flow in z-coordinate ocean models. J. Phys. Oceanogr. 28, 2163–2174.